

Hierarchical time crystals

Jan Carlo Schumann,^{1,*} Igor Lesanovsky,^{1,2} and Parvinder Solanki^{1,†}

¹ Institut für Theoretische Physik and Center for Integrated Quantum Science and Technology, Universität Tübingen, Auf der Morgenstelle 14, 72076 Tübingen, Germany

²School of Physics and Astronomy and Centre for the Mathematics and Theoretical Physics of Quantum Non-Equilibrium Systems, University of Nottingham, Nottingham, NG7 2RD, United Kingdom

(Dated: January 16, 2026)

Spontaneous symmetry breaking is one of the central organizing principles in physics. Time crystals have emerged as an exotic phase of matter, spontaneously breaking the time translational symmetry, and are mainly categorized as discrete or continuous. While these distinct types of time crystals have been extensively explored as standalone systems, intriguing effects can arise from their mutual interaction. Here, we demonstrate that a time-independent coupled system of discrete and continuous time crystals induces a simultaneous two-fold temporal symmetry breaking, resulting in a *hierarchical time crystal* phase. Interestingly, one of the subsystems breaks an emergent discrete temporal symmetry that does not exist in the dynamical generator but rather emerges dynamically, leading to a convoluted non-equilibrium phase. We demonstrate that hierarchical time crystals are robust, emerging for fundamentally different coupling schemes and persisting across wide ranges of system parameters.

Introduction.— Spontaneous symmetry breaking (SSB), where the stable state of a system lacks a symmetry respected by its dynamical generator [1], shapes phases of matter across scales – from macroscopic phenomena in cosmology [2–5] to the smallest scales of nuclear and particle physics [6–8]. In many-body quantum systems, SSB has emerged as a unifying framework for organizing both equilibrium and non-equilibrium phenomena [9–13]. Striking manifestations of SSB are time crystal phases, where a many-body system spontaneously breaks the time translational symmetry of the underlying generator of the dynamics [14–19]. Depending on the nature of the broken temporal symmetry, time crystals can be mainly categorized as discrete (DTC) [20–32] or continuous (CTC) [33–49] time crystals. A DTC constitutes a phase of matter that breaks the underlying discrete temporal symmetry of its generator. The subharmonic oscillations that emerge here become robust as the system size diverges [17, 18, 50]. On the other hand, a CTC features persistent oscillations even in the complete absence of time-dependent external fields, breaking the continuous time translational symmetry [33].

All standalone time crystal setups investigated so far only break a single temporal symmetry. While the interplay between multiple, nested symmetries has recently garnered interest in many-body systems [51–53], its implications for temporal symmetries remain limited to time-dependent closed quantum systems [54].

In this work, we demonstrate that distinct temporal symmetries can be broken simultaneously in a time-independent system, giving rise to a convoluted phase of matter, which we term a *hierarchical time crystal* (HTC). To uncover this intriguing phenomenon, we consider a coupled system comprising a CTC and a DTC (displayed

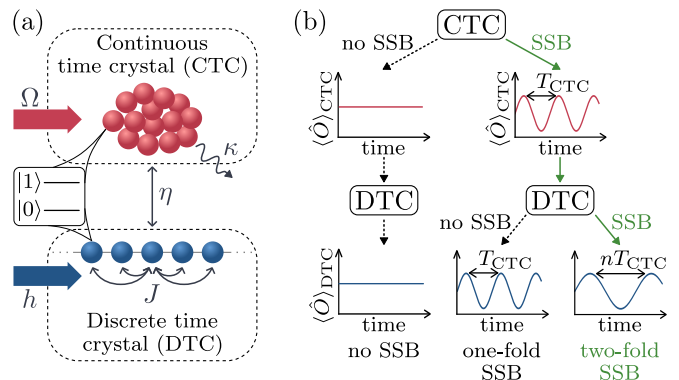


FIG. 1. **Sketch of the model and hierarchical symmetry breaking.** (a) The time-independent coupled time crystal model features a CTC subsystem, realized as a collective spin ensemble, which interacts with a DTC subsystem of long-range coupled spins at interaction strength η . Each spin-1/2 system consists of a ground state $|0\rangle$ and an excited state $|1\rangle$. Both CTC and DTC are subjected to constant drives with strength Ω and h , respectively, with the CTC additionally exhibiting collective emission at a rate κ . (b) Illustration of spontaneous symmetry breaking (SSB) possibilities: no SSB, where the observables $\langle \hat{O} \rangle_\alpha$ are time-independent for both CTC and DTC; one-fold SSB, where only the CTC breaks a temporal symmetry, leading to synchronized periodic oscillations of both DTC and CTC with period T_{CTC} ; and two-fold SSB, where the DTC discretely breaks the emergent periodicity of the CTC phase, leading to subharmonic oscillations with a period $T_{\text{DTC}} = nT_{\text{CTC}}$. The latter phase is termed a hierarchical time crystal (HTC).

in Fig. 1(a)). Here, the underlying hierarchical breaking of multiple time translational symmetries unfolds in two steps, as illustrated in Fig. 1(b). First, the CTC can spontaneously break the continuous time translational symmetry of the time-independent composite system,

leading to an emergent periodic oscillatory phase. The hereby emerging time-periodicity of the CTC can then, in turn, be broken discretely by the DTC, manifesting in a sub-harmonic response to the CTC phase (green path in Fig. 1(b)). Interestingly, the DTC breaks a symmetry that is absent in the underlying dynamical generator, but rather one that emerges dynamically, thereby establishing an intricate non-equilibrium phase of matter, characterized by nested temporal order.

To analyze this nested phase in time, we employ the relative frequency between the CTC and DTC as an order parameter, as it captures the frequency locking behavior between two subsystems. Remarkably, in the sub-harmonic frequency locking regime of the DTC subsystem, we observe both integer and fractional multiples of the CTC period. This locking phenomenon does not require fine-tuning; instead, it features multiple plateaus of distinct locking frequencies spanning over a range of system parameters, resulting in a staircase-like structure associated with higher-order synchronization phenomena [55–57]. We demonstrate that the emerging HTC phase is robust against parameter variations, quantum fluctuations, and fundamentally different coupling mechanisms between the time crystals, encompassing both coherent and dissipative interactions. The associated concept of hierarchical symmetry breaking extends beyond merely temporal symmetries, introducing a broader framework of hierarchical dissipative phase transitions.

HTC model.— To investigate the emergence of an HTC, we analyze a coupled system of a CTC and a DTC, governed by the Lindblad master equation

$$\dot{\hat{\rho}} = \mathcal{L}_{\text{HTC}}\hat{\rho} = (\mathcal{L}_{\text{DTC}} + \mathcal{L}_{\text{CTC}} + \mathcal{L}_{\text{Int}})\hat{\rho}. \quad (1)$$

Here, \mathcal{L}_{DTC} and \mathcal{L}_{CTC} describe the dynamics of the uncoupled DTC and CTC subsystem, respectively, while \mathcal{L}_{Int} accounts for their mutual interaction. The combined Liouvillian \mathcal{L}_{HTC} entails the dynamics of the composite system.

We now consider specific examples for each subsystem. For the CTC, we choose the well-known boundary time crystal model [33]. It consists of a collection of N_{C} spin-1/2 systems that are subject to a constant drive at strength Ω and experience collective dissipation at rate κ (cf. top panel in Fig. 1(a)). Consequently, the CTC dynamics is governed by the following Lindblad dynamical generator

$$\mathcal{L}_{\text{CTC}}\hat{\rho} = -i\Omega[\hat{S}_{\text{C}}^x, \hat{\rho}] + \frac{\kappa}{S_{\text{C}}}\mathcal{D}[\hat{S}_{\text{C}}^z]\hat{\rho}, \quad (2)$$

where $\mathcal{D}[\hat{O}]\hat{\rho} = \hat{O}\hat{\rho}\hat{O}^\dagger - \frac{1}{2}\{\hat{O}^\dagger\hat{O}, \hat{\rho}\}$ denotes the dissipator and we set $\hbar = 1$. The total spin of the CTC subsystem is given by $S_{\text{C}} = N_{\text{C}}/2$, and the collective spin operators are defined as $\hat{S}_{\text{C}}^\alpha = \sum_{i=1}^N \hat{\sigma}_{i,\text{C}}^\alpha/2$, where $\hat{\sigma}_{i,\text{C}}^\alpha$ are the Pauli spin matrices of the i -th atom in direction $\alpha \in \{x, y, z\}$. The ladder operators are defined as $\hat{S}_{\text{C}}^\pm = \hat{S}_{\text{C}}^x \pm i\hat{S}_{\text{C}}^y$. In

the thermodynamic limit $N \rightarrow \infty$, the system transitions from a stationary state in the strongly dissipative regime ($\Omega/\kappa < 1$) to an oscillatory phase in the weakly dissipative regime ($\Omega/\kappa > 1$), breaking the generator's continuous time translational symmetry. This dissipative phase transition manifests in the closing of the Liouvillian spectral gap [58] as the system size diverges, with the emergence of purely imaginary eigenvalues for the time crystal phase [33, 35, 59].

For the DTC subsystem, we choose a variant of the Lipkin–Meshkov–Glick (LMG) model [60–62], which is known to develop a robust subharmonic response under periodic driving [22, 30]. In particular, it consists of a chain of N_{D} spin-1/2 systems that are connected via long-range interactions at strength J (cf. Fig. 1(a)). Here, we consider the case of a static drive at strength h , where the system's dynamics can be described by a Lindblad generator of the form

$$\mathcal{L}_{\text{DTC}}\hat{\rho} = -i \left[-\frac{2J}{S_{\text{D}}}(\hat{S}_{\text{D}}^z)^2 - h\hat{S}_{\text{D}}^x, \hat{\rho} \right]. \quad (3)$$

Here, the collective DTC spin operators, $S_{\text{D}}^{x,y,z,\pm}$, are defined analogously to the CTC case, where the subscript D (C) refers to the DTC (CTC) subsystem. The parameters J and h set the collective interaction strength and the constant drive strength, respectively. For simplicity, we assume in the following that both subsystems contain the same number of constituents, N , such that $S_{\text{C}} = S_{\text{D}} = N/2$. After detailing the specific time-crystal models, we explore how various coupling schemes influence the emergence of HTCs in the upcoming sections.

Coherent coupling.— We begin by analyzing a coherent coupling scheme, $\mathcal{L}_{\text{Int}}\hat{\rho} = -i[\hat{H}_{\text{Int}}, \hat{\rho}]$, where

$$\hat{H}_{\text{Int}} = \frac{\eta}{2iN} \left(\underbrace{\hat{S}_{\text{C}}^+ \hat{S}_{\text{D}}^+ - \hat{S}_{\text{C}}^- \hat{S}_{\text{D}}^-}_{\text{counter-rotating}} + \underbrace{\hat{S}_{\text{C}}^+ \hat{S}_{\text{D}}^- - \hat{S}_{\text{C}}^- \hat{S}_{\text{D}}^+}_{\text{co-rotating}} \right). \quad (4)$$

This interaction Hamiltonian establishes a bilinear coupling between two collective spins, allowing for both excitation exchange (co-rotating terms) and simultaneous excitation creation/annihilation (counter-rotating terms). To understand the effect of this interaction term on the breaking of hierarchical symmetries of the coupled system, we first investigate the mean-field dynamics considering the thermodynamic limit $N \rightarrow \infty$. In particular, we study the time evolution of the expectation values of the rescaled collective spin operators $m_i^\alpha \equiv \langle \hat{m}_i^\alpha \rangle = 2\langle \hat{S}_i^\alpha \rangle/N$, assuming the factorization of expectation values due to vanishing correlations such that $\langle \hat{m}_i^\alpha \hat{m}_j^\beta \rangle = \langle \hat{m}_i^\alpha \rangle \langle \hat{m}_j^\beta \rangle$.

To observe HTCs, we consider the weak dissipation regime ($\Omega/\kappa > 1$) of the CTC, corresponding to its symmetry-broken time crystal phase where the observables $m_{\text{C}}^{x,y,z}$ begin to oscillate with a finite frequency

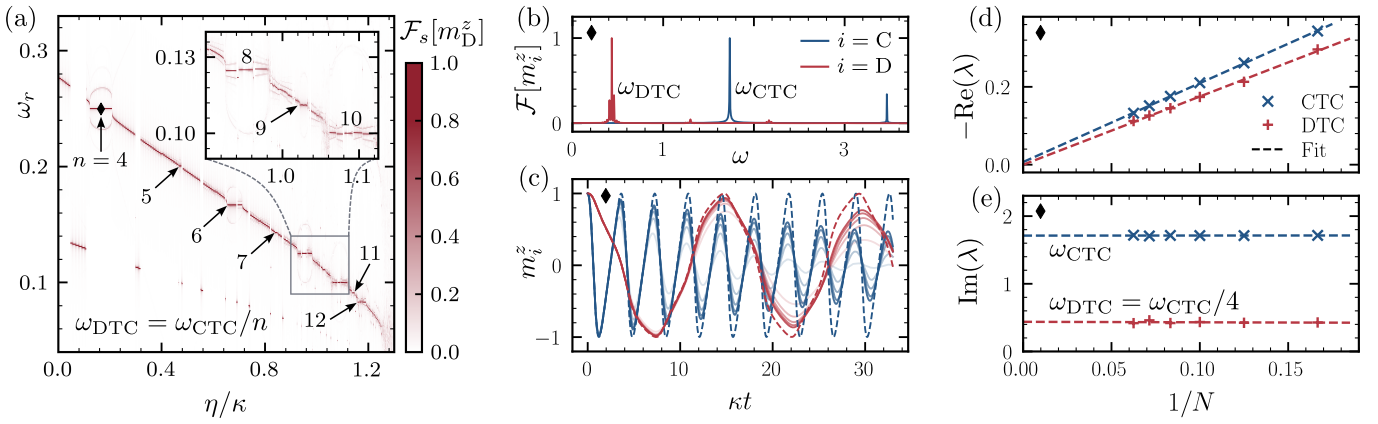


FIG. 2. Hierarchical symmetry breaking via coherent coupling. In panel (a), stroboscopic Fourier amplitudes of the DTC magnetization z component $\mathcal{F}_s[m_D^z]$ are plotted against the rescaled inter-TC coupling strength η/κ . The relative frequency $\omega_r = \omega_{\text{DTC}}/\omega_{\text{CTC}}$ exhibits distinct locking plateaus at integer values for the DTC order n , where $\omega_{\text{DTC}}(\omega_{\text{CTC}})$ represents the dominant frequency of DTC (CTC). System parameters are fixed to $\Omega/\kappa = 2$, $J/\kappa = 0.1$, and $h/\kappa = 0.25$, while the initial state is $(m_{\text{C},\text{D}}^x, m_{\text{C},\text{D}}^y, m_{\text{C},\text{D}}^z) = (0, 0, 1)$. The main panel (inset) probes m_D^z over 1000 (3000) CTC periods. The HTC phase for the specific case of a 4-DTC (diamond in (a)) is detailed in panels (b-e). Panel (b) presents the normalized Fourier spectrum $\mathcal{F}[m_i^z]$ of both CTC (blue) and DTC (red). The respective dominant frequencies are labeled. In panel (c), the time evolution of m_C^z (blue) and m_D^z (red) is displayed for finite system sizes $N \in \{20, 40, \dots, 100\}$ with ascending opacity, which approaches the mean-field solutions indicated with dashed lines. Panels (d) and (e) show the dependence of the real and imaginary parts of the dominant Liouvillian eigenvalues on the system size. The dashed lines indicate linear fits to the CTC and DTC eigenvalues, confirming the spectral gap closure with purely imaginary eigenvalues, which match the frequencies obtained from the mean-field analysis in panel (b).

ω_{CTC} (cf. Fig. 1(b)) [33]. In this setting, the CTC essentially functions as an emergent periodic drive for the DTC, and the coupling parameter η takes on the role of the corresponding effective drive strength. The DTC further breaks the emergent periodicity and develops subharmonic oscillations. To characterize the associated HTC phase, we consider the ratio of the oscillation frequencies $\omega_r = \omega_{\text{DTC}}/\omega_{\text{CTC}}$ as an order parameter, since it captures whether the DTC sub-harmonically locks to the CTC phase. Here, ω_{DTC} denotes the dominant DTC frequency.

The frequency responses of the subsystems can be accessed by Fourier transformations of the signals obtained from numerically solving the mean field equations (see Supplemental Material (SM) [63]). The resulting stroboscopic Fourier amplitudes over a range of values of the coupling strength η are displayed in Fig. 2(a). Indeed, distinct plateaus of constant DTC frequency emerge with respect to the CTC frequency such that $\omega_{\text{DTC}} = \omega_{\text{CTC}}/n$, resulting in a staircase-like structure for the order parameter ω_r with respect to the coupling strength η . The corresponding order n of the n -DTC (black in Fig. 2(a)) prominently exhibits integer values in the range $n = 4 - 12$ (see SM [63] for an example of fractional locking). These stable plateaus indicate robust subharmonic frequency locking behavior, thereby facilitating the emergence of an HTC.

To further understand this frequency locking of the DTC with respect to the CTC, we investigate the normalized

Fourier amplitudes of the subsystems. The system parameters are fixed to correspond to a stable frequency locking plateau. This is exemplarily shown in Fig. 2(b) for a 4-DTC (cf. diamond marker in Fig. 2(a)). One observes sharp dominant peaks confirming the subharmonic relation, while occurring secondary peaks corresponding to higher harmonics and indicating non-linear oscillations are significantly smaller, resulting in subtle aperiodic signatures atop the subharmonic response. To further illustrate the robustness of the HTC phase, we verify that the system continues to exhibit frequency locking over a broad range of DTC interaction and drive parameters, J and h , maintaining the stability of the associated plateaus (see SM [63]).

Next, we go beyond the mean-field limit to finite system sizes N in order to study quantum fluctuations that are inevitable in finite systems. Remarkably, the observed HTC phase remains robust to inter-system back-action and intrinsic quantum fluctuations. To reach this insight, we numerically solve Eq. (1) for different N . Note that for the calculations, we can restrict ourselves to the symmetric spin- $N/2$ (Dicke) subspace, since the system's total spin is conserved. Additionally, we choose the system parameters such that we operate in a previously found stable n -DTC regime, namely $n = 4$ (cf. diamond marker in Fig. 2(a)). The resulting magnetization trajectories for both CTC (blue) and DTC (red) in Fig. 2(c) clearly exhibit the predicted fourfold increase of the DTC period with respect to the CTC for all system sizes. Fur-

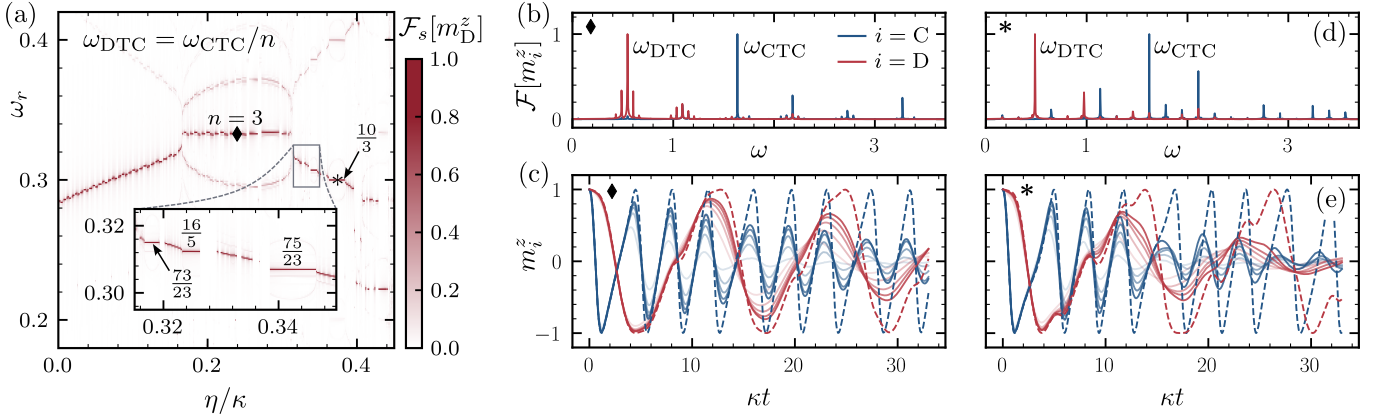


FIG. 3. Hierarchical symmetry breaking via dissipative coupling. (a) Stroboscopic Fourier amplitudes of the DTC magnetization z component $\mathcal{F}_s[m_D^z]$ are plotted against the rescaled inter-TC coupling strength η/κ . The dominant component of the relative frequency ω_r exhibits distinct locking plateaus at both integer and fractional values for the DTC order n . System parameters are fixed to $\Omega/\kappa = 2$, $J/\kappa = 0.08$, and $h/\kappa = 0.2522$, while the initial state is $(m_{C,D}^x, m_{C,D}^y, m_{C,D}^z) = (0, 0, 1)$. The main panel and inset probe m_D^z over 1000 and 3000 CTC periods, respectively. The system parameters are chosen to target a (b,c) 3-DTC (diamond in (a)) and a (d,e) fractional 10/3-DTC (star in (a)), respectively. (b),(d) Normalized Fourier spectra of both CTC (blue) and DTC (red) with labeled dominant frequencies. (c),(e) Time evolution of m_C^z (blue) and m_D^z (red) for finite system sizes $N \in \{20, 40, \dots, 100\}$ displayed in ascending opacity, approaching the dashed lines indicating the corresponding mean field solution.

thermore, the individual trajectories decay exponentially with a system-size-dependent rate but converge towards the mean-field solutions (corresponding dashed lines) as the system size diverges. Such a closing of the spectral gap in the Liouvillian eigenvalues, where the eigenvalues' real parts vanish, constitutes another hallmark of time crystals [33, 58].

To showcase the associated dissipative phase transition, we thus analyze the eigenspectra of \mathcal{L}_{HTC} in Eq. (1) for finite system sizes. In particular, we focus on the dominant eigenvalues of the CTC and DTC subsystems responsible for the observed dynamics in Fig. 2(c). They can be distinguished by the imaginary and real parts matching the trajectories' oscillation frequency and exponential decay rate, respectively. On the one hand, the real parts displayed in Fig. 2(d) obey the expected power-law decay with increasing system size. An additional linear fit to the data reveals the vanishing behavior of the decay rate in the thermodynamic limit, leading to infinitely long-lived oscillations. On the other hand, the evolution of the imaginary parts in Fig. 2(e) takes a constant form, thus decoupling the frequency of the oscillations from the system size. The corresponding linear fit offsets for both CTC and DTC match the dominant angular frequencies identified in Fig. 2(b), respectively. These findings underline the clear subharmonic character of the DTC oscillations with respect to the CTC across all system sizes, confirming the simultaneous breaking of temporal symmetries for finite N . Furthermore, the emergence of stable HTC phases is not confined to this specific type of coherent coupling, as the SM [63] shows for coherent spin-exchange coupling.

Dissipative coupling and fractional HTC.— The HTC phase emerges independently of the nature of the coupling. To showcase this, we consider collective dissipation as an incoherent coupling scheme, characterized by the Liouvillian,

$$\mathcal{L}_{\text{Int}}\hat{\rho} = \frac{2\eta}{N} \mathcal{D}[\hat{S}_C^- + \hat{S}_D^-]\hat{\rho}. \quad (5)$$

Analogous to the preceding section, we begin by analyzing the emerging mean-field dynamics while fixing the CTC in its symmetry-broken phase. Similar to the coherent coupling, one observes constant plateaus for the order parameter ω_r that span over finite ranges of the coupling strength η , as shown in Fig. 3(a). Note that the stable locking regimes also persist under variations of the remaining DTC parameters (see SM [63]), confirming the stability of the emergent DTC phase.

However, a key qualitative difference compared to coherent coupling lies in the emergence of fractional n -DTC phases, defined by the relation $n = p/q$, where p and q are coprime integers. To better understand this new feature, we compare the Fourier spectra resulting from an integer and a fractional DTC phase. Specifically, we focus on the integer 3-DTC and fractional 10/3-DTC plateaus from Fig. 3(a) (diamond and star marker), where the corresponding normalized spectra are displayed in Figs. 3(b) and (d), respectively. Analogous to the discussion of coherent coupling, in the case of integer locking, the spectra reveal sharp peaks at dominant frequencies for both subsystems. This results in nicely behaved oscillations for both DTC and CTC as observed in Fig. 3(c). Conversely, for fractional locking, more secondary peaks

with significant magnitude coexist alongside the dominant peaks, rendering highly non-linear oscillations, as depicted in Fig. 3(e). This richness in dynamics stems from the higher-order synchronization feedback between subsystems with fractional frequencies, resulting in intricate magnetization trajectories.

A similar effect can be observed even for finite system size trajectories for both fractional and integer cases, which approach the mean-field solutions as the system size diverges. Therefore, we confirm the emergence of HTC for dissipative coupling and the validity of mean-field results by performing a finite-size analysis of the exact master equation. This further confirms that the emergence of HTC phases is not limited to a particular interaction scheme, but is rather inevitable, even for incoherent collective dissipative coupling.

Conclusion.— Our findings unveil a mechanism for inducing nested temporal order in non-equilibrium many-body systems. In particular, we identified and characterized hierarchical time crystals (HTC) and the underlying hierarchical breaking of temporal symmetries in an interacting open quantum system composed of two distinct types of time crystals: continuous and discrete. We demonstrated that the continuous-time translational symmetry broken by the CTC gives rise to an emergent period that is itself discretely broken by the DTC, resulting in two-fold symmetry breaking and, consequently, a stable HTC phase. Additionally, we showed that this intriguing HTC phase remains robust against parameter variations, quantum fluctuations, and fundamentally different coupling schemes, including both dissipative and coherent mechanisms. The intriguing phenomenon of hierarchical symmetry breaking can be explored in existing cavity QED setups that have successfully realized the effective LMG Hamiltonian used for the DTC model [64] and the open Dicke model, which leads to a CTC phase [65]. Alternatively, interacting Bose–Einstein condensate systems provide a complementary platform, where tunable collisional and light-mediated interactions have been shown to realize both DTC [66] and CTC phases [45], paving the way for the experimental observation of nested temporal order and, hence, hierarchical dissipative phase transitions.

Acknowledgments. P.S. acknowledges support from the Alexander von Humboldt Foundation through a Humboldt research fellowship for postdoctoral researchers. I.L. acknowledges support from the QuantERA II programme (project CoQuaDis, DFG Grant No. 532763411) that has received funding from the EU H2020 research and innovation programme under GA No. 101017733. I.L. also acknowledges funding from the Deutsche Forschungsgemeinschaft (DFG, German Research Foundation) through the Research Unit FOR 5413/1, Grant No. 465199066, from the Leverhulme Trust (Grant No. RPG-2024-112) and from the European Union through the ERC grant OPEN-2QS (Grant No. 101164443). J.S.

acknowledges support from the Deutschlandstipendium for committed students.

* jan.schumann@student.uni-tuebingen.de

† parvinder@mnf.uni-tuebingen.de

- [1] A. J. Beekman, L. Rademaker, and J. van Wezel, An introduction to spontaneous symmetry breaking, *SciPost Phys. Lect. Notes*, **11** (2019).
- [2] G. B. Gelmini, M. Gleiser, and E. W. Kolb, Cosmology of biased discrete symmetry breaking, *Phys. Rev. D* **39**, 1558 (1989).
- [3] A. Giovannakis, *Spontaneous symmetry breaking: From the effective action to cosmological phase transitions in the standard model and beyond* (2024), arXiv:2407.00807 [hep-ph].
- [4] A. Albrecht and P. J. Steinhardt, Cosmology for grand unified theories with radiatively induced symmetry breaking, *Phys. Rev. Lett.* **48**, 1220 (1982).
- [5] G. G. Raffelt, Spontaneous symmetry breaking in supernova neutrinos, *Nucl. and Part. Phys. Proc.* **265–266**, 81 (2015).
- [6] S. Frauendorf, Spontaneous symmetry breaking in rotating nuclei, *Rev. Mod. Phys.* **73**, 463 (2001).
- [7] P. W. Higgs, Broken symmetries and the masses of gauge bosons, *Phys. Rev. Lett.* **13**, 508 (1964).
- [8] Y. Nambu, Spontaneous symmetry breaking in particle physics: A case of cross fertilization, *Nobel Lectures In Physics (2006–2010)* **3**, 191 (2014).
- [9] P. W. Anderson, More is different, *Science* **177**, 393 (1972).
- [10] T. Brauner, Spontaneous symmetry breaking and nambu–goldstone bosons in quantum many-body systems, *Symmetry* **2**, 609 (2010).
- [11] G. Morandi, Spontaneous symmetry breaking in quantum many-body systems (A solid-state physicist’s view of Goldstone’s theorem and all that), *Pramana* **25**, 419 (1985).
- [12] M. C. Cross and P. C. Hohenberg, Pattern formation outside of equilibrium, *Rev. Mod. Phys.* **65**, 851 (1993).
- [13] D. V. Else, C. Monroe, C. Nayak, and N. Y. Yao, Discrete time crystals, *Ann. Rev. Cond. Matter Phys.* **11**, 467 (2020).
- [14] F. Wilczek, Quantum time crystals, *Phys. Rev. Lett.* **109**, 160401 (2012).
- [15] P. Bruno, Impossibility of spontaneously rotating time crystals: A no-go theorem, *Phys. Rev. Lett.* **111**, 070402 (2013).
- [16] H. Watanabe and M. Oshikawa, Absence of quantum time crystals, *Phys. Rev. Lett.* **114**, 251603 (2015).
- [17] K. Sacha and J. Zakrzewski, Time crystals: a review, *Rep. Prog. Phys.* **81**, 016401 (2017).
- [18] K. Sacha, *Time crystals*, Vol. 114 (Springer, 2020).
- [19] V. Khemani, R. Moessner, and S. L. Sondhi, *A brief history of time crystals* (2019), arXiv:1910.10745 [cond-mat.str-el].
- [20] K. Chinzei and T. N. Ikeda, Criticality and rigidity of dissipative discrete time crystals in solids, *Phys. Rev. Res.* **4**, 023025 (2022).
- [21] D. V. Else, B. Bauer, and C. Nayak, Floquet time crystals, *Physical Review Letters* **117**, 10.1103/phys

- revlett.117.090402 (2016).
- [22] A. Pizzi, J. Knolle, and A. Nunnenkamp, Higher-order and fractional discrete time crystals in clean long-range interacting systems, *Nat. Commun.* **12**, 2341 (2021).
- [23] A. Pizzi, A. Nunnenkamp, and J. Knolle, Classical prethermal phases of matter, *Phys. Rev. Lett.* **127**, 140602 (2021).
- [24] Z. Gong, R. Hamazaki, and M. Ueda, Discrete time-crystalline order in cavity and circuit qed systems, *Phys. Rev. Lett.* **120**, 040404 (2018).
- [25] F. M. Gambetta, F. Carollo, M. Marcuzzi, J. P. Garrahan, and I. Lesanovsky, Discrete time crystals in the absence of manifest symmetries or disorder in open quantum systems, *Phys. Rev. Lett.* **122**, 015701 (2019).
- [26] K. Chinzei and T. N. Ikeda, Time crystals protected by floquet dynamical symmetry in hubbard models, *Phys. Rev. Lett.* **125**, 060601 (2020).
- [27] C.-h. Fan, D. Rossini, H.-X. Zhang, J.-H. Wu, M. Artoni, and G. C. La Rocca, Discrete time crystal in a finite chain of rydberg atoms without disorder, *Phys. Rev. A* **101**, 013417 (2020).
- [28] B. Zhu, J. Marino, N. Y. Yao, M. D. Lukin, and E. A. Demler, Dicke time crystals in driven-dissipative quantum many-body systems, *New J. Phys.* **21**, 073028 (2019).
- [29] L. Oberreiter, U. Seifert, and A. C. Barato, Subharmonic oscillations in stochastic systems under periodic driving, *Phys. Rev. E* **100**, 012135 (2019).
- [30] A. Russomanno, F. Iemini, M. Dalmonte, and R. Fazio, Floquet time crystal in the lipkin-meshkov-glick model, *Phys. Rev. B* **95**, 214307 (2017).
- [31] J. Zhang, P. W. Hess, A. Kyprianidis, P. Becker, A. Lee, J. Smith, G. Pagano, I.-D. Potirniche, A. C. Potter, A. Vishwanath, N. Y. Yao, and C. Monroe, Observation of a discrete time crystal, *Nature* **543**, 217 (2017).
- [32] B. Liu, L.-H. Zhang, Q.-F. Wang, Y. Ma, T.-Y. Han, J. Zhang, Z.-Y. Zhang, S.-Y. Shao, Q. Li, H.-C. Chen, B.-S. Shi, and D.-S. Ding, Higher-order and fractional discrete time crystals in Floquet-driven Rydberg atoms, *Nat. Commun.* **15**, 9730 (2024).
- [33] F. Iemini, A. Russomanno, J. Keeling, M. Schirò, M. Dalmonte, and R. Fazio, Boundary time crystals, *Phys. Rev. Lett.* **121**, 035301 (2018).
- [34] G. Buonaiuto, F. Carollo, B. Olmos, and I. Lesanovsky, Dynamical phases and quantum correlations in an emitter-waveguide system with feedback, *Phys. Rev. Lett.* **127**, 133601 (2021).
- [35] F. Carollo and I. Lesanovsky, Exact solution of a boundary time-crystal phase transition: Time-translation symmetry breaking and non-markovian dynamics of correlations, *Phys. Rev. A* **105**, L040202 (2022).
- [36] M. Hajdušek, P. Solanki, R. Fazio, and S. Vinjanampathy, Seeding crystallization in time, *Phys. Rev. Lett.* **128**, 080603 (2022).
- [37] M. Krishna, P. Solanki, M. Hajdušek, and S. Vinjanampathy, Measurement-induced continuous time crystals, *Phys. Rev. Lett.* **130**, 150401 (2023).
- [38] B. Buča and D. Jaksch, Dissipation induced nonstationarity in a quantum gas, *Phys. Rev. Lett.* **123**, 260401 (2019).
- [39] K. Seibold, R. Rota, and V. Savona, Dissipative time crystal in an asymmetric nonlinear photonic dimer, *Phys. Rev. A* **101**, 033839 (2020).
- [40] P. Solanki, M. Krishna, M. Hajdušek, C. Bruder, and S. Vinjanampathy, Exotic synchronization in continuous time crystals outside the symmetric subspace, *Phys. Rev. Lett.* **133**, 260403 (2024).
- [41] M. Jirasek, I. Lesanovsky, and A. Cabot, The boundary time crystal as a light source for quantum enhanced sensing beyond the Heisenberg limit (2025), arXiv:2511.23416 [quant-ph].
- [42] K. Tucker, B. Zhu, R. J. Lewis-Swan, J. Marino, F. Jimenez, J. G. Restrepo, and A. M. Rey, Shattered time: can a dissipative time crystal survive many-body correlations?, *New J. Phys.* **20**, 123003 (2018).
- [43] F. Russo and T. Pohl, Quantum dissipative continuous time crystals, *Phys. Rev. Lett.* **135**, 110404 (2025).
- [44] Y. Huang, T. Wang, H. Yin, M. Jiang, Z. Luo, and X. Peng, Observation of continuous time crystals and quasi-crystals in spin gases, *Nat. Commun.* **16**, 9375 (2025).
- [45] P. Kongkhambut, J. Skulte, L. Mathey, J. G. Cosme, A. Hemmerich, and H. Keßler, Observation of a continuous time crystal, *Science* **377**, 670 (2022), <https://www.science.org/doi/pdf/10.1126/science.abo3382>.
- [46] B. Liu, L.-H. Zhang, Y. Ma, Q.-F. Wang, T.-Y. Han, J. Zhang, Z.-Y. Zhang, S.-Y. Shao, Q. Li, H.-C. Chen, G.-C. Guo, D.-S. Ding, and B.-S. Shi, Bifurcation of time crystals in driven and dissipative Rydberg atomic gas, *Nat. Commun.* **16**, 1419 (2025).
- [47] P. Solanki and F. Minganti, Chaos as a manifestation of time-translation symmetry breaking, *Phys. Rev. B* **112**, 134311 (2025).
- [48] P. Solanki, A. Cabot, M. Brunelli, F. Carollo, C. Bruder, and I. Lesanovsky, Generation of entanglement and non-stationary states via competing coherent and incoherent bosonic hopping, *Phys. Rev. A* **112**, L030601 (2025).
- [49] Z. Wang, R. Gao, X. Wu, B. Buča, K. Mølmer, L. You, and F. Yang, Boundary time crystals induced by local dissipation and long-range interactions, *Phys. Rev. Lett.* **135**, 230401 (2025).
- [50] M. P. Zaletel, M. Lukin, C. Monroe, C. Nayak, F. Wilczek, and N. Y. Yao, Colloquium: Quantum and classical discrete time crystals, *Rev. Mod. Phys.* **95**, 031001 (2023).
- [51] R. M. Nandkishore and M. Hermele, Fractons, *Ann. Rev. Cond. Matter Phys.* **10**, 295 (2019).
- [52] M. Pretko, X. Chen, and Y. You, Fracton phases of matter, *Int. J. Mod. Phys. A* **35**, 2030003 (2020).
- [53] B. C. Rayhaun and D. J. Williamson, Higher-form subsystem symmetry breaking: Subdimensional criticality and fracton phase transitions, *SciPost Phys.* **15**, 017 (2023).
- [54] Z. Fu, R. Moessner, H. Zhao, and M. Bukov, Engineering hierarchical symmetries, *Phys. Rev. X* **14**, 041070 (2024).
- [55] M. H. Jensen, P. Bak, and T. Bohr, Complete devil's staircase, fractal dimension, and universality of mode-locking structure in the circle map, *Phys. Rev. Lett.* **50**, 1637 (1983).
- [56] B. Lingnau, K. Shortiss, F. Dubois, F. H. Peters, and B. Kelleher, Universal generation of devil's staircases near hopf bifurcations via modulated forcing of nonlinear systems, *Phys. Rev. E* **102**, 030201 (2020).
- [57] X. Wu, Y. Zhang, J. Peng, S. Boscolo, C. Finot, and H. Zeng, Farey tree and devil's staircase of frequency-locked breathers in ultrafast lasers, *Nat. Commun.* **13**, 5784 (2022).
- [58] F. Minganti, A. Biella, N. Bartolo, and C. Ciuti, Spec-

- tral theory of liouvillians for dissipative phase transitions, *Phys. Rev. A* **98**, 042118 (2018).
- [59] A. Cabot, L. S. Muhle, F. Carollo, and I. Lesanovsky, Quantum trajectories of dissipative time crystals, *Phys. Rev. A* **108**, L041303 (2023).
- [60] H. Lipkin, N. Meshkov, and A. Glick, Validity of many-body approximation methods for a solvable model: (i). exact solutions and perturbation theory, *Nucl. Phys.* **62**, 188 (1965).
- [61] N. Meshkov, A. Glick, and H. Lipkin, Validity of many-body approximation methods for a solvable model: (ii). linearization procedures, *Nucl. Phys.* **62**, 199 (1965).
- [62] A. Glick, H. Lipkin, and N. Meshkov, Validity of many-body approximation methods for a solvable model: (iii). diagram summations, *Nucl. Phys.* **62**, 211 (1965).
- [63] See the Supplemental Material for information on the HTC stability regimes and a discussion of an additional coherent coupling scheme.
- [64] N. Sauerwein, F. Orsi, P. Uhrich, S. Bandyopadhyay, F. Mattiotti, T. Cantat-Moltrecht, G. Pupillo, P. Hauke, and J.-P. Brantut, Engineering random spin models with atoms in a high-finesse cavity, *Nat. Phys.* **19**, 1128 (2023).
- [65] E. Y. Song, D. Barberena, D. J. Young, E. Charparro, A. Chu, S. Agarwal, Z. Niu, J. T. Young, A. M. Rey, and J. K. Thompson, A dissipation-induced superradiant transition in a strontium cavity-qed system, *Science Advances* **11**, eadu5799 (2025), <https://www.science.org/doi/pdf/10.1126/sciadv.adu5799>.
- [66] H. Keßler, P. Kongkhambut, C. Georges, L. Mathey, J. G. Cosme, and A. Hemmerich, Observation of a dissipative time crystal, *Phys. Rev. Lett.* **127**, 043602 (2021).

SUPPLEMENTAL MATERIAL

Hierarchical time crystals

Jan Carlo Schumann,¹ Igor Lesanovsky,^{1,2} and Parvinder Solanki¹

¹*Institut für Theoretische Physik and Center for Integrated Quantum Science and Technology,
Auf der Morgenstelle 14, 72076 Tübingen, Germany*

²*School of Physics and Astronomy and Centre for the Mathematics
and Theoretical Physics of Quantum Non-Equilibrium Systems,
The University of Nottingham, Nottingham, NG7 2RD, United Kingdom*

In this Supplemental Material, we present detailed mean-field calculations and stability analyses for the coherent and incoherent coupling schemes described in the main text. We also include the analysis of hierarchical symmetry breaking for an additional coherent coupling scheme.

I. MEAN-FIELD EQUATIONS AND STABILITY REGIMES FOR COHERENT COUPLING

In this section, we present a detailed discussion of the mean-field results for the coherent coupling scheme outlined in the main text. We also analyze the stability regimes of the hierarchical time crystal (HTC) phase with respect to various parameters.

Mean-field equations

The time evolution of an observable \hat{O} can be given by the following equation

$$\begin{aligned} \frac{d}{dt}\langle\hat{O}\rangle &= \frac{d}{dt}\text{Tr}\left(\hat{\rho}\hat{O}\right) = \text{Tr}\left(\mathcal{L}^\dagger\hat{O}\right) \\ &= i\text{Tr}\left([\hat{H},\hat{O}]\hat{\rho}\right) + \sum_i \frac{\gamma_i}{2}\text{Tr}\left(([\hat{L}_i^\dagger,\hat{O}]\hat{L}_i + \hat{L}_i^\dagger[\hat{O},\hat{L}_i])\hat{\rho}\right), \end{aligned} \quad (\text{S1})$$

where we inserted the Lindblad master equation in the second step and used the cyclic property of the trace to rearrange the terms. Here, \hat{H} denotes the system Hamiltonian, \hat{L}_i the i -th jump operator and γ_i the corresponding decay rate. For the considered coherent coupling scheme, the total Hamiltonian reads

$$\hat{H} = \Omega\hat{S}_C^x - \frac{4J}{N}(\hat{S}_D^z)^2 - h\hat{S}_D^x + \underbrace{\frac{\eta}{2iN}\left(\hat{S}_C^+\hat{S}_D^+ - \hat{S}_C^-\hat{S}_D^- + \hat{S}_C^+\hat{S}_D^- - \hat{S}_C^-\hat{S}_D^+\right)}_{\hat{H}_{\text{Int}}}. \quad (\text{S2})$$

Note that by plugging in the definition of the spin raising and lowering operators $\hat{S}_j^\pm = \hat{S}_j^x \pm i\hat{S}_j^y$, the expression for the interaction Hamiltonian can be simplified to $\hat{H}_{\text{Int}} = 2\eta\hat{S}_C^y\hat{S}_D^x/N$. In the considered setting, we only have one jump operator $\hat{L}_1 = \hat{S}_C^-$ with corresponding decay rate $\gamma_1 = 2\kappa/N$. We now consider $\hat{O} = \hat{m}_i^\alpha$ with the rescaled collective spin operators $\hat{m}_i^\alpha = 2\hat{S}_i^\alpha/N$ introduced in the main text, where $\alpha \in \{x, y, z\}$ and $i \in \{C, D\}$. In the thermodynamic limit $N \rightarrow \infty$, these operators commute, since

$$\left\|[\hat{m}_j^\alpha, \hat{m}_k^\beta]\right\| = \frac{\delta_{jk}}{N}i\epsilon^{\alpha\beta\gamma}\left\|\hat{m}_j^\gamma\right\| \xrightarrow{N \rightarrow \infty} 0. \quad (\text{S3})$$

We assume vanishing correlations, defining the mean-field limit together with $N \rightarrow \infty$, such that

$$\langle\hat{m}_j^\alpha\hat{m}_k^\beta\rangle = \langle\hat{m}_j^\alpha\rangle\langle\hat{m}_k^\beta\rangle. \quad (\text{S4})$$

Calculating Eq. (S1) for the rescaled collective spin operators using that their expectation values factor in the mean-field limit yields a set of coupled nonlinear differential equations for their expectation values $m_i^\alpha \equiv \langle\hat{m}_i^\alpha\rangle$.

These mean-field equations define the dynamics of the system in the thermodynamic limit. For the specified coherent coupling scheme, one obtains:

$$\begin{aligned}
\frac{d}{dt}m_C^x &= \eta m_C^z m_D^x + \kappa m_C^z m_C^x \\
\frac{d}{dt}m_C^y &= -\Omega m_C^z + \kappa m_C^z m_C^y \\
\frac{d}{dt}m_C^z &= \Omega m_C^y - \eta m_C^x m_D^x - \kappa ((m_C^x)^2 + (m_C^y)^2) \\
\frac{d}{dt}m_D^x &= 4J m_D^z m_D^y \\
\frac{d}{dt}m_D^y &= -\eta m_C^y m_D^z + 2h m_D^z - 4J m_D^z m_D^x \\
\frac{d}{dt}m_D^z &= \eta m_C^y m_D^y - 2h m_D^y .
\end{aligned} \tag{S5}$$

Stability regimes

In the main text, we demonstrated the emergence of hierarchical symmetry breaking for finite ranges of the inter-TC coupling strength η , depicted in Fig. 2(a) of the main text. We now investigate the robustness of the associated HTC phase with respect to other parameters of this model, in particular, the all-to-all interaction strength J and the constant drive strength h of the DTC subsystem.

To this end, we first examine the stability of the locking plateaus in Fig. 2(a) of the main text as J is varied while h is kept fixed. In particular, we highlight the parameter regimes where we observe stable subharmonic locking of the DTC to the CTC phase. This is displayed in Fig. S1(a), where the marker color indicates the order n of the corresponding n -DTC. Following this logic, uni-colored areas directly correspond to frequency locking, which is stable to perturbations of the system parameters. Indeed, one observes contiguous patches of distinct colors, indicating that the locking behavior is robust to variations in the parameter J and is not fine-tuned to particular values chosen in the main text.

Furthermore, staircase structures, such as Fig. 2(a) of the main text, which illustrates the frequency locking steps, are merely a horizontal cut at the corresponding J value. For the shown cut at $\eta/\kappa = 0.15$ (dashed horizontal line in Fig. S1(a)), one receives the stroboscopic Fourier amplitudes displayed in Fig. S1(b). Here, the intervals where the DTC sub-harmonically locks to the CTC phase exactly match the predictions from Fig. S1(a), for example, illustrated with dotted vertical lines for the 6-DTC. To reobtain Fig. 2(a) in the main text, one performs the horizontal cut at $J/\kappa = 0.1$, crossing different stability areas with $n \in \{4, 5, \dots, 12\}$, manifesting in the rich staircase-like structure. Therefore, one can extract the form of the staircase of the relative frequency ω_r for different parameter values from such stability regime diagrams. This also entails predictions for no locking behavior, e.g., for $J/\kappa = 0.22$ in Fig. S1(a), since a horizontal cut does not cross any stability areas.

Analogously, in Fig. S1(c), we fix the inter-DTC coupling strength J and repeat the above-described procedure while varying the DTC drive strength h . Again, we find stable locking regimes that span finite parameter ranges of h and η , thereby confirming the stable many-body phase. As discussed above, Fig. 2(a) of the main text can be obtained by a horizontal cut at $h/\kappa = 0.25$. Cutting at $h/\kappa = 0.45$ yields the Fourier amplitudes displayed in Fig. S1(d). As expected, all predicted locking steps from Fig. S1(c) can be found. Interestingly, an additional fractional locking step emerges at $\eta/\kappa \approx 0.92$ with $n = 8/3$. The corresponding stability region is not shown in Figs. S1(c) as it only contains information about integer values of n . In both panels (a,b) of Fig. S1, we find that stability regimes corresponding to higher DTC orders n are generally more sensitive to parameter fluctuations. This can be seen from the decreasing area of the locking regimes for higher n values.

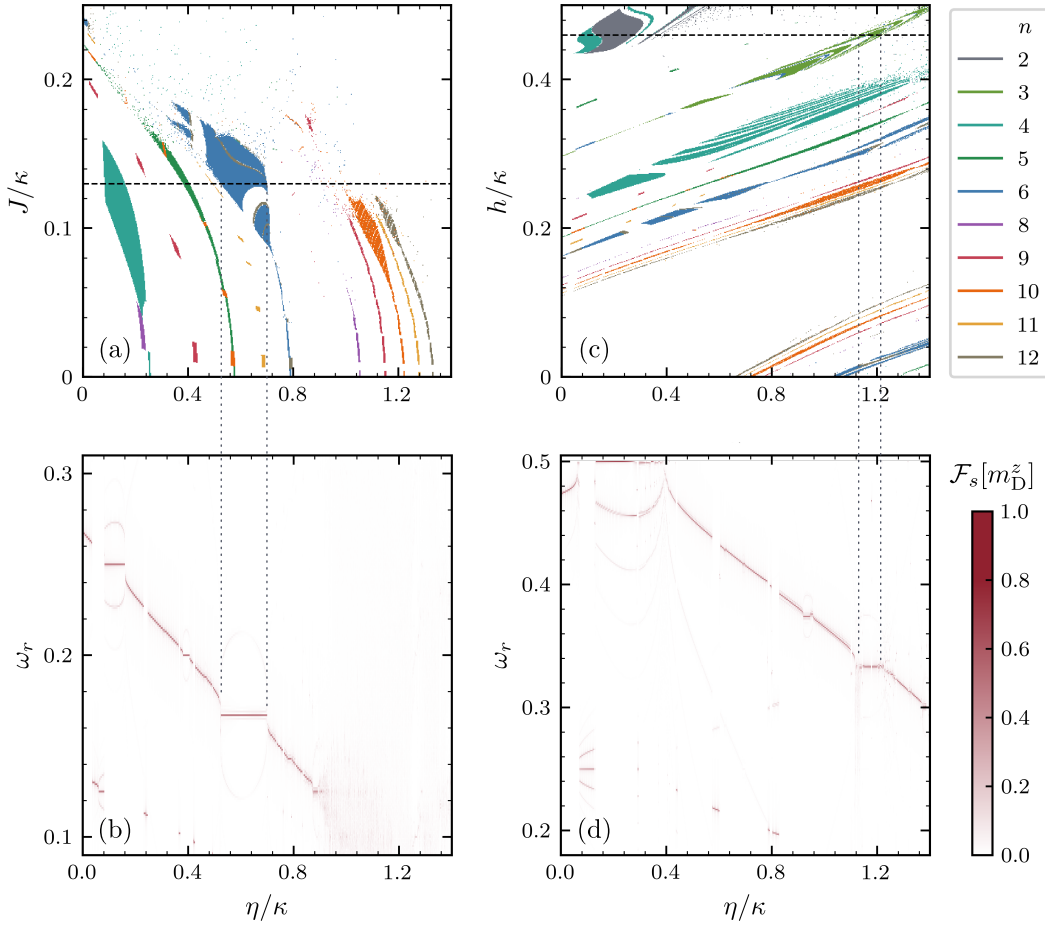


FIG. S1. **HTC parameter regimes for coherent coupling.** (a,c) Stroboscopic Fourier amplitudes of the corresponding n -DTC, which exceed 0.5, are marked in their respective color. The CTC drive strength is fixed at $\Omega/\kappa = 2$, while the initial state is $(m_{C,D}^x, m_{C,D}^y, m_{C,D}^z) = (0, 0, 1)$. (a) DTC all-to-all interaction strength J/κ vs. inter-TC coupling strength η/κ with $h/\kappa = 0.25$. (c) DTC drive strength h/κ vs. inter-TC coupling strength η/κ with $J/\kappa = 0.1$. (b,d) Stroboscopic Fourier amplitudes of the DTC magnetization z component $\mathcal{F}_s[m_D^z]$ are plotted against the inter-TC coupling strength η/κ for a fixed parameter set. The CTC is fixed in its time crystal regime with $\Omega/\kappa = 2$ and m_D^z is probed over 1000 CTC periods. (b) Fixed DTC all-to-all interaction strength at $J/\kappa = 0.125$ corresponding to the dashed line in (a). Locking intervals of η/κ coincide with the predicted intervals in (a), as exemplarily visualized with grey dotted lines for the 6-DTC. (d) Fixed DTC drive strength at $h/\kappa = 0.45$ corresponding to the dashed line in (c). The in (c) predicted locking intervals are clearly distinguishable (e.g. grey dotted lines for the 3-DTC). Additionally, a new, fractional locking plateau emerges at $\eta/\kappa \approx 0.92$, which has not been tracked in panel (c).

II. DISSIPATIVE COUPLING

Analogous to Appendix I, this section provides the mean-field equations and HTC stability regimes for dissipative coupling. As described in the main text, the system Hamiltonian in this setting is given as

$$\hat{H} = \Omega \hat{S}_C^x - \frac{4J}{N} (\hat{S}_D^z)^2 - h \hat{S}_D^x. \quad (\text{S6})$$

As for the previously discussed case of coherent coupling, we consider the jump operator $\hat{L}_1 = \hat{S}_C^-$ with decay rate $\gamma_1 = 2\kappa/N$. Additionally, we include a second jump operator $\hat{L}_2 = \hat{S}_C^- + \hat{S}_D^-$ with decay rate $\gamma_2 = 2\eta/N$, which induces incoherent coupling between the time crystals. Plugging this in Eq. (S1) for the rescaled collective spin operators \hat{m}_i^α

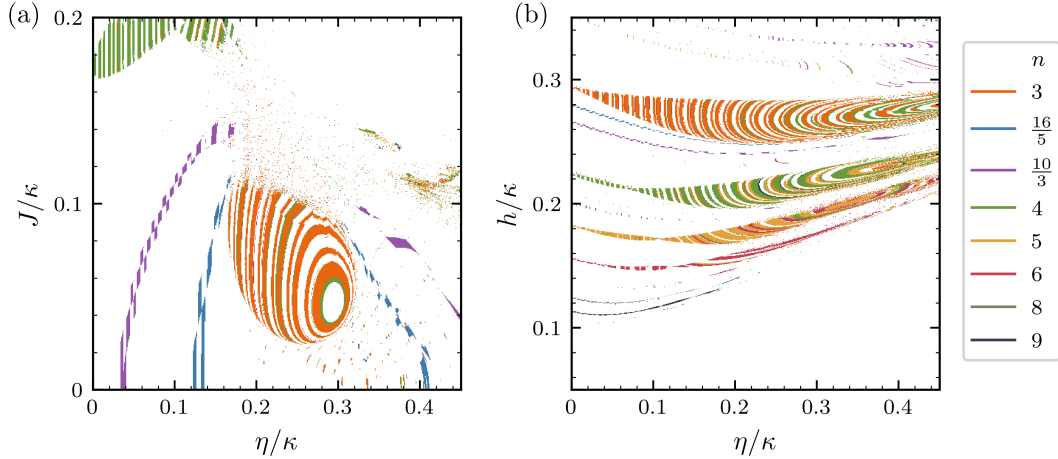


FIG. S2. **HTC parameter regimes for dissipative coupling.** Relative Fourier amplitudes of the corresponding n -DTC, which exceed 0.5, are marked in their respective color. The CTC drive strength is fixed at $\Omega/\kappa = 2$, while the initial state is $(m_{C,D}^x, m_{C,D}^y, m_{C,D}^z) = (0, 0, 1)$. (a) DTC all-to-all interaction strength J/κ vs. inter-TC coupling strength η/κ . (b) DTC drive strength h/κ vs. inter-TC coupling strength η/κ .

as explained in Appendix I yields the mean-field equations. One obtains

$$\begin{aligned}
 \frac{d}{dt}m_C^x &= \kappa m_C^x m_C^z + \eta m_C^z (m_C^x + m_D^x) \\
 \frac{d}{dt}m_C^y &= \kappa m_C^y m_C^z - \Omega m_C^z + \eta m_C^z (m_C^y + m_D^y) \\
 \frac{d}{dt}m_C^z &= \Omega m_C^y - \kappa ((m_C^x)^2 + (m_C^y)^2) - \eta (m_C^y (m_C^y + m_D^y) + m_C^x (m_C^x + m_D^x)) \\
 \frac{d}{dt}m_D^x &= 4J m_D^z m_D^y + \eta m_D^z (m_D^x + m_D^x) \\
 \frac{d}{dt}m_D^y &= \eta m_D^z (m_D^y + m_D^y) + 2h m_D^z - 4J m_D^z m_D^x \\
 \frac{d}{dt}m_D^z &= -2h m_D^y - \eta (m_D^y (m_D^y + m_D^y) + m_D^x (m_D^x + m_D^x)).
 \end{aligned} \tag{S7}$$

To investigate the HTC stability regimes, we mark parameter sets that correspond to stable subharmonic frequency locking of the DTC with respect to the CTC. The result is displayed in Fig. S2, where we investigate the dependence on the inter-DTC interaction strength J and the DTC drive strength h in panels (a) and (b), respectively. As discussed above, the locking step behavior displayed in Fig. 3(a) in the main text can be obtained by a horizontal cut at $J/\kappa = 0.08$ in Fig. S2(a), or equivalently at $h/\kappa = 0.2522$ in Fig. S2(b). As expected, one finds continuous areas of one color in both panels of Fig. S2, most prominently for the 3-DTC (orange) and 4-DTC (green), which indicate stable n -DTC, and therefore HTC phases. In Fig. S2(a), stable areas of locking to fractional multiples of the CTC period are also clearly distinguishable (blue and purple). The corresponding fractional DTC phases are, however, notably more sensitive to variations of h as evident from Fig. S2(b). Interestingly, in both subplots, a seemingly larger area of stable locking is intersected by thin strips where the locking breaks down, forming, for example, a honeycomb-like structure. Nevertheless, we confirm the stability of the subharmonic response across finite ranges of the system parameters, and with that, the stable HTC phase.

III. SPIN-EXCHANGE COUPLING

In this section, we discuss an additional coherent coupling scheme, namely spin-exchange coupling. Here, the two subsystems can exchange an excitation coherently. Analogous to the discussed coupling schemes in the main text, it

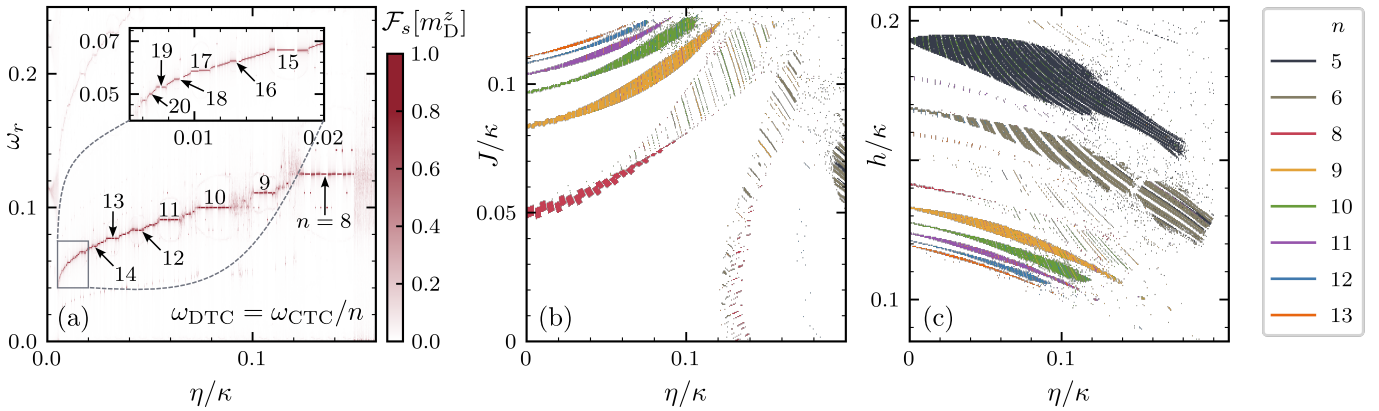


FIG. S3. Hierarchical symmetry breaking via spin-exchange coupling in the mean-field limit. (a) Relative Fourier amplitudes of the DTC magnetization z component $\mathcal{F}_s[m_D^z]$ are plotted against the rescaled inter-TC coupling strength η/κ . The dominant component of the relative frequency ω_r exhibits distinct locking plateaus at both integer and fractional values for the DTC order n . System parameters are set to $\Omega/\kappa = 2$, $J/\kappa = 0.1157$, and $h/\kappa = 0.115$, while the initial state is $(m_{C,D}^x, m_{C,D}^y, m_{C,D}^z) = (0, 0, 1)$. The main panel and inset probe $mz2$ over 1000 and 3000 CTC periods, respectively. (b,c) Stability regimes under variation of the DTC all-to-all interaction strength J and drive strength h , respectively. Relative Fourier amplitudes of the corresponding n -DTC, which exceed 0.5, are marked in their respective color.

is modulated by the inter-TC coupling strength η . The interaction Hamiltonian thus reads

$$\hat{H}_{\text{Int}} = \frac{2\eta}{N} \left(\hat{S}_C^+ \hat{S}_D^- + \hat{S}_C^- \hat{S}_D^+ \right), \quad (\text{S8})$$

which leads to the interaction Liouvillian $\mathcal{L}_{\text{Int}} = -i[\hat{H}_{\text{Int}}, \hat{\rho}]$. We analyze the emergence of HSB for the given choice of interaction scheme through both mean-field and finite system size analysis. First, we focus on the mean-field limit to get an overview of the system's dynamics. The mean-field equations for the given coupling scheme take the form

$$\begin{aligned} \frac{d}{dt} m_C^x &= 2\eta m_C^z m_D^y + \kappa m_C^z m_C^x \\ \frac{d}{dt} m_C^y &= -\Omega m_C^z - 2\eta m_C^z m_D^x + \kappa m_C^z m_C^y \\ \frac{d}{dt} m_C^z &= \Omega m_C^y + 2\eta(m_C^y m_D^x - m_C^x m_D^y) - \kappa((m_C^x)^2 + (m_C^y)^2) \\ \frac{d}{dt} m_D^x &= 4J m_D^z m_D^y + 2\eta m_D^z m_C^y \\ \frac{d}{dt} m_D^y &= -2\eta m_D^z m_C^x + 2h m_D^z - 4J m_D^z m_D^x \\ \frac{d}{dt} m_D^z &= 2\eta(m_D^y m_C^x - m_D^x m_C^y) - 2h m_D^y. \end{aligned} \quad (\text{S9})$$

To identify HSB, we stick with the ratio of the subsystem oscillation frequencies ω_r as an order parameter, introduced in the main text and obtained via Fourier transformations of the mean-field solutions $m_i^\alpha(t)$. Displayed in Fig. S3(a), constant plateaus where the DTC frequency locks to a subharmonic frequency of the CTC emerge. Interestingly, while for the considered coherent and dissipative coupling schemes in the main text, the order n of the locking plateaus increased with growing coupling strength η , the opposite behavior is observed here.

Notably, higher DTC orders, given by n , are observed compared to the discussed coupling schemes in the main text, reaching up to $n = 20$. For lower DTC orders, we verify that the found stable HTC phases persist under variation of the remaining DTC parameters, namely the all-to-all interaction strength J and the constant drive h . This can be seen in Fig. S3(b) and (c), where points corresponding to stable subharmonic frequency locking are marked, while the color indicates the DTC order n . Again, one finds stability areas with respect to different parameters, confirming the robust nature of the many-body HTC phase. In conclusion, we have demonstrated that spin-exchange coupling also gives rise to hierarchical time translational symmetry breaking and, consequently, a stable HTC phase.